Efficient photocatalytic hydrogen evolution over carbon supported antiperovskite cobalt zinc nitride

Efficient photocatalytic hydrogen evolution over carbon supported antiperovskite cobalt zinc nitride

Siqi Liu [a,b], Xiangjian Meng [a,b], Samira Adimi [a,b], Haichuan Guo [a,b], Weiliang Qi [a,b,*], J. Paul Attfield [c,*], and Minghui Yang [a,b *]

[a] *Ningbo Institute of Materials Technology & Engineering, Chinese Academy of Sciences, Ningbo 315201, P.R. China.*

[b] *Center of Materials Science and Optoelectronics Engineering, University of Chinese Academy of Sciences, Beijing 100049, P.R. China.*

[c] *Centre for Science at Extreme Conditions and School of Chemistry, University of Edinburgh, King's Buildings, Edinburgh, UK.*

*Correspondence Author: Prof. Minghui Yang, Prof. J. Paul Attfield, Dr. Weiliang Qi;

E-mail addresses: myang@nimte.ac.cn, j.p.attfield@ed.ac.uk, qiweiliang@nimte.ac.cn;

Abstract

Photocatalytic solar to chemical energy conversion is an important energy conversion process but suffer from low efficiency. Thus, development of efficient photocatalytic system using earth-abundant elements with low costs is highly desirable. Here, antiperovskite cobalt zinc nitride has been synthesized and coupled with carbon black (Co_3ZnN/C) for visible light driven hydrogen production in an Eosin Y-sensitized system. Replacement of cobalt atom by zinc atom leads to an improved charge transfer kinetics and catalytic properties compared with Co_4N. Density functional theory (DFT) calculations further reveal the adjusted electronic structure of Co_3ZnN by zinc atom introducing. The lower antibonding energy states of Co_3ZnN are beneficial for the hydrogen desorption. Moreover, carbon black as support effectively reduces the particle size of Co_3ZnN and benefits to the electron storage and adsorption capabilities. The optimal Co_3ZnN/C catalysts exhibit the H_2 evolution rate of 15.4 μmol mg^{-1} h^{-1}, which is over 6 times higher than that of monometallic Co_4N. It is even greater than those of most of Eosin Y-sensitized systems.

Keywords: Transition metal nitride; Antiperovskite materials; Particle-size control; Carbon support; Hydrogen evolution;

1. Introduction

Solar to chemical energy conversion is a potential way to meet the urgent demand for renewable and clean energy [1, 2]. So far, noble metal-based materials are generally considered as the best photocatalyst or co-catalyst due to their small over-potential and unique electronic structures [3, 4]. However, limited natural abundance restricts their application on a large scale [5]. In this case, continuative exploitation of efficient and stable alternative non-noble-metal based photocatalytic systems has great significance. Recent developments in transition metal nitrides (TMNs) materials supply a new direction for selecting non-noble-metal based catalysts [6, 7]. Compared to other materials, TMNs have attracted widespread interest due to their high chemical stability and low electrical resistance [8, 9]. The d-bands of the TMNs produce a contraction compared to their parent metals which causes a greater density of states (DOS) near the Fermi level [10]. The redistributions by the DOS in TMNs give them similar properties to group VIII noble metal materials [11]. Therefore, TMNs-based materials have shown their potential for solar to chemical energy conversion in the field of photocatalysis [12, 13].

Recently, cobalt-based nitrides have been reported as multifunctional catalysts for both photocatalytic hydrogen evolution and CO_2 reduction due to their unique electronic properties [14]. However, because of the harsh synthetic conditions, monometallic cobalt nitrides generally exhibit large particle size with low surface area and less active sites [15, 16]. Thus, the photocatalytic efficiency of monometallic cobalt nitrides-based catalysts is insufficient. Further optimizations of cobalt-based nitrides in components, structures as well as morphologies are highly desirable to develop novel TMNs-based photocatalyst with superior efficiency. The properties of metallic atoms heavily affect the catalytic properties of TMNs materials [17, 18]. Introducing another metallic atom with suitable atomic radius and electronic properties, forming

bimetallic cobalt-based nitrides is considered to be effective for improving the catalytic efficiency of cobalt nitrides [19].

Here, we report a bimetallic cobalt-zinc nitride (Co_3ZnN) coupled with carbon black (Co_3ZnN/C) for Eosin Y-sensitized photocatalytic hydrogen evolution under visible light irradiation. Zinc atoms replace the cobalt atoms at the apex of the cubic unit cell forming antiperovskite phase Co_3ZnN with improved electronic properties as compared to Co_4N. Density functional theory (DFT) calculations reveal the adjusted electronic structure of Co_3ZnN by zinc atom introducing. The lower antibonding energy states of Co_3ZnN are beneficial for the hydrogen desorption. Moreover, using carbon black as a support, the particle size of Co_3ZnN has been effectively reduced to the nanometer scale. It leads to increased adsorption and electronic storage capabilities of Co_3ZnN/C. Therefore, Co_3ZnN/C exhibits the highest H_2 evolution rate of 15.4 μmol mg^{-1} h^{-1}, which is over 6 times higher than that of monometallic Co_4N. In fact, it is superior as compared with most cobalt-based materials systems and other non-precious metal-based systems.

2. Results and discussion

As illustrated in **Scheme S1**, a series of transition metal nitrides (TMNs) have been synthesized by nitriding the nitrate precursors (**Fig. S1**) at 600 °C for 1 h. XRD Rietveld refinement analysis confirms the successful formation of cubic phase Co_4N and Co_3ZnN without crystalline impurities (**Fig. 1a** and **Fig. 1b**). Interestingly, Co_3ZnN exhibits an antiperovskite structure which endows it a diverse array of unconventional physical and chemical properties as reported before [20-22]. Since the electronegativity of Zn is smaller than N and Co, the substitution of Co at A-site in Co_4N using Zn increased the electron density between B-site N

and X-site Co. Because the electrical conduction in the perovskite-structured compound is mostly contributed by the B-X-B network, the substitution could lead to better conductivity. In fact, Co_3ZnN even exhibits lower electrical resistance than commercial carbon black (**Fig. S2**). It indicates the superior electronic transfer properties of Co_3ZnN as compared to that of Co_4N. In addition, DFT calculated charge density distribution results further confirm the advantages of Co_3ZnN with antiperovskite structure. As shown in **Fig. 1c-d**, a more negative charge can be observed at N-Co-N network in Co_3ZnN than that in Co_4N, which contributes better electrical conduction. Co_3ZnN/C nanocomposites show similar crystalline phase with Co_3ZnN except for additional diffraction peak for carbon black (**Fig. S3**). According to the computing results of the Debye-Scherrer equation, the size of crystalline grain for Co_3ZnN gradually decreases as the carbon content increases. It is consistent with the results of morphology analysis by electron microscopes. As shown in **Fig. 2a** and **Fig. S4**, pure Co_3ZnN exhibits an irregular bulk morphology with the size around 200-400 nm, which is pretty similar to that of Co_4N. The large size is likely inherited from its precursor (**Fig. S1**), which forms by shrinkage of the larger sized precursor samples. The high-resolution transmission electron microscopy (HRTEM) image reveals two interplanar spacing of 0.265 nm and 0.216 nm in Co_3ZnN (**Fig. 2b**), corresponding to the (110) and (111) plane, respectively. It is in agreement with XRD results. After introducing carbon black as a support, the size of Co_3ZnN can be successfully modulated. As shown in **Fig. S5** and **Fig. 2c**, the Co_3ZnN/C maintains the morphology and size of the carbon black. The particle size of Co_3ZnN in Co_3ZnN/C is substantially reduced to 20-30 nm. Besides, the intimate contact between Co_3ZnN nanoparticles and carbon black can be found in **Fig. 2d**, which benefits the electrons transfer capability of Co_3ZnN/C.

The compositions and chemical states of the three catalysts are further confirmed by X-ray photoelectron spectroscopy (XPS) and Raman spectra (**Fig. 3** and **Fig. S6**). The high-resolution spectrum of Co 2p in **Fig. 3a** depicts Co 2p orbitals and two corresponding satellites. The fitted high-resolution Co 2p spectra of the three different catalysts all present three forms of Co species. For the Co_4N sample, the dominant peaks at 782.84 eV and 801.60 eV are from Co^{3+} coordinated to O or N ions, and are attributed to the transition metal nitride phase [19, 23]. The metallic Co^0 (Co-Co) can be seen at 778.86 eV and 795.25 eV, and the Co^{2+} coordinated to O which appears at 780.85 eV and 797.22 eV [24, 25]. The inevitable oxidation on the surface of transitional metal nitride with metallic characteristics leads to such surface states. The ultrathin oxidized layer protects the transition metal nitrides from further oxidation and does not offer any discernible hindrance to fast electron transport [16]. The peaks of Co^0 and Co^{3+} exhibit a negative shift for Co_3ZnN compared with Co_4N, indicating the tunable electronic structure after the accession of zinc [26]. As carbon black are introduced into the system of Co_3ZnN, the peaks of Co^0 and Co^{3+} shift to the higher binding energy. It reveals the charge transfer to the transition metal nitride is taking place [27]. The similar shift trend of Zn 2p binding energies of these two catalysts further confirms this process (**Fig. 3b**). The N 1s peaks can be deconvoluted into two for Co_4N, corresponding to N-Co (397.19 eV) and N-O (399.60 eV), which proves that it is essentially a metal nitride (**Fig. 3c**) [17, 28]. The new peak at 397.99 eV for Co_3ZnN is considered as N-Zn bonds, further confirms this unique bimetallic structure [29]. In the Raman spectrum of Co_4N (**Fig. 3d**), four Raman bands centered at 470, 510 and 607, as well as 675 cm^{-1} correspond to the E_g, F_{2g}, and A_{1g} vibration modes of CoO_x, respectively [30]. It is in agreement with the inevitable surface oxidation of TMNs, which has also been confirmed by XPS results. A new Raman peak observed at 692 cm^{-1} for Co_3ZnN has been assigned to the A_{1g} vibration modes

of the $ZnCo_2O_4$ phase, which further confirms the form of bimetallic structure [31]. After adding carbon black, the Raman peaks have no change suggest the major structures of Co_3ZnN are preserved in the composites.

The photocatalytic activities of as-prepared TMNs samples for hydrogen production are estimated in an Eosin Y-sensitized system under visible light irradiation. All the TMNs samples in the absence of Eosin Y are not active under identical conditions (**Fig. S7a**), indicating that the photoactivity for H_2 evolution is driven by electrons from the light excitation of Eosin Y sensitizer. As shown in **Fig. 4a**, due to the large particle size and less exposed active sites, the H_2-generation rate of monometallic nitrides Co_4N is only 2 μmol mg^{-1} h^{-1}. Bimetallic nitride Co_3ZnN exhibits obviously superior catalytic performance (7.2 μmol mg^{-1} h^{-1}) as compared to that of Co_4N, due to its modulated electronic structure by Zn and excellent electron transfer capability caused by its antiperovskite structure. After optimization by introduction of carbon black as support, a series of Co_3ZnN/C samples show better catalytic performance than those of Co_3ZnN and Co_4N (**Fig. S7b**). Notably, much loading amount of carbon black would lead to the gradually reduced activity, which could be ascribed to the reduction of reactive sites (Co_3ZnN) for hydrogen evolution in the Co_3ZnN/C nanocomposites. With further optimizing reaction conditions (**Fig. S7c-d**), the optimal Co_3ZnN/C(1:1) sample shows H_2 generation rate of 15.4 μmol mg^{-1} h^{-1}, which is superior as compared to most previous reported cobalt-based catalysts (**Table S2**). In fact, this result is even better than those of most previous reported photocatalytic Eosin Y-sensitized systems with none-noble-metal catalysts (**Table S3**).

Photo-stability is important to the practical applications of the catalysts. Therefore, the photo-stability of Co_3ZnN/C(1:1) has been tested. As shown in **Fig. S8a**, Co_3ZnN/C(1:1) shows that around 28.8 % of activity loss has been found after five cycles of reaction tests. It is due to the

consumption of the TEOA and Eosin Y in the systems (**Fig. S8b**). After 5 cycles, $Co_3ZnN/C(1:1)$ has been collected and washed by water and ethanol several times. By supplementing the same amounts of the TEOA and Eosin Y, the reclaimed $Co_3ZnN/C(1:1)$ exhibits a similar H_2 evolution rate as compared to that of the first cycle, suggesting the fine stability of $Co_3ZnN/C(1:1)$ (**Fig. S9a**). In addition, XRD and SEM analysis have also been tested to further confirm the stability of $Co_3ZnN/C(1:1)$. As shown in **Fig. S9b**, $Co_3ZnN/C(1:1)$ exhibits similar crystal structure before and after reaction. SEM image of reclaimed $Co_3ZnN/C(1:1)$ after reaction displays similar morphology with that of fresh $Co_3ZnN/C(1:1)$ (**Fig. S9c**). Therefore, it can be concluded that $Co_3ZnN/C(1:1)$ shows excellent photo-stability in Eosin Y-sensitized systems during visible light irradiation.

Owing to the introduction of carbon black, a high specific area for Co_3ZnN/C can be expected. As shown in **Table S1** and **Fig. S10**, $Co_3ZnN/C(1:1)$ exhibits an extremely high surface area (114.20 $m^2\ g^{-1}$) and pore volume (0.21 $cm^3\ g^{-1}$) compared with bulk Co_4N (3.01 $m^2\ g^{-1}$ and 0.021$cm^3\ g^{-1}$) and Co_3ZnN (3.50 $m^2\ g^{-1}$ and 0.021$cm^3\ g^{-1}$). The introduction of carbon black increased the specific surface area of the sample by approximately 33 times. Thus, $Co_3ZnN/C(1:1)$ has the best ability to adsorb Eosin Y in three samples (**Fig. S11**). Moreover, although all the three catalysts show full band absorption, Co_3ZnN/C composite has the strongest optical absorption capacity (**Fig. S12**). All the advantages of adding carbon black may further promote the photocatalytic activity of Co_3ZnN.

To decipher the original reasons for the promoted photocatalytic activity of bimetallic nitride Co_3ZnN and Co_3ZnN/C nanocomposites, a series of photoluminescence (PL) and electrochemical studies are conducted. Co_3ZnN exhibits a lower PL intensity than Co_4N (**Fig. S13**), suggesting a more prominent suppression of the recombination of electron and excited

state of Eosin Y [32, 33]. The introduction of carbon black further boosts this suppression effect. The polarization curves reveal an evidently higher current density for Co_3ZnN than Co_4N (**Fig. 4b**), indicating improved charge transfer kinetics by the bimetallic structure of Co_3ZnN [34]. Co_3ZnN/C(1:1) sample displays the highest current density and lowest over-potential, which is attributed to the fact that the spatial distribution of Co_3ZnN in the composites enables the exposure of more available active sites on the Co_3ZnN surface [35]. Electrochemical impedance spectroscopy (EIS) spectra are shown in **Fig. 4c**, Co_3ZnN exhibits an improved charge transfer compared with the Co_4N. Surprisingly, although the electrochemical impedance of pure carbon black is higher than that of the Co_3ZnN, the combination of carbon black and Co_3ZnN shows the most efficient charge transfer [36]. This further proves the synergistic effect between carbon black and Co_3ZnN.

Co_3ZnN reveals a larger area enclosed than the Co_4N in **Fig. S14**, which suggests Zinc atoms in the system of antiperovskite can facilitate electronic storage (the inset of **Fig. S14**). When adding carbon black in the system of Co_3ZnN, the specific capacitance of the sample gets a theatrical boost compared with pure Co_3ZnN. As such, it is reasonable to claim that the electrons from the photoexcitation of Eosin Y can be further stored by nitrogen-doped carbon black of the composite [37]. Meanwhile, the bimetallic nitride Co_3ZnN has a high electrochemical double-layer capacitance (C_{dl} = 0.054 mF/cm^2) than that of monometallic nitride Co_4N (C_{dl} = 0.038 mF/cm^2), indicating cobalt and zinc bimetallic structure exposes more active sites for reactions than cobalt monometallic structure (**Fig. S15**) [38]. It also provides another powerful explanation for the excellent performance of bimetallic nitride Co_3ZnN. Although the Co_3ZnN/C composite shows a more exaggerated capacitance enhanced, combined with the low photocatalytic activity

of carbon black (only 1.7 μmol/h), which indicates that the carbon black is generally as electronic storage stations rather than active sites.

In addition, hydrogen temperature programmed desorption (TPD) of Co_4N and Co_3ZnN/C have been tested. As shown in **Fig. 4d**, Co_4N exhibits a small H_2 desorption peak at about 182 °C and then a broad H_2 desorption peak at 340 °C. These results indicate that there exist at least two sites on the Co_4N surface for H_2 chemisorption: weak and strong chemisorption sites. For Co_3ZnN/C, desorption temperatures from both sites evidently decrease to 167 °C and 250 °C, respectively. The decrease in desorption temperatures means that the adsorbed hydrogen species have weaker interactions with Co_3ZnN/C surface and thus have a higher reactivity. Moreover, a new sharp peak at 439 °C has also been observed. It suggests a new strong chemisorption site in Co_3ZnN/C as compared to that of Co_4N. From the TPD results, the substitution of Co at A-site in Co_4N using Zn could obviously increase the active sites for H_2 chemisorption but weakens the interactions of atomic hydrogen with Co_3ZnN/C surface [39].

Density functional theory (DFT) calculations are carried out to further confirm the origin of the excellent photoactivity of TMNs materials. The optimized structural representations of Co_4N and Co_3ZnN are presented in **Fig. 5a-b**. The band structure of the two samples calculated with Perdew-Burke-Ernzerhof (PBE) functional is shown in **Fig. 5c-d**, it reveals the metallic features of these two metal nitrides [40]. The valence bands of both samples have passed through Fermi level (zero) to enter their conduction bands, illustrating the existence of free electrons near the Fermi level, in good agreement with the density of states (DOS) plots, shown in **Fig. 5e-f**, indicating the metallic nature of both samples [41, 42]. Moreover, the electronic interaction, coupling the Co and N valence states with the Zn d-states in Co_3ZnN, is clear from these plots. The PDOS contributed to the p orbitals of Nitrogen atoms are successive, suggesting a covalent

interaction among Co, Zn, and N in the energy region between -5 to -8 eV, far below the Fermi level. Unique cobalt and zinc bimetallic structure lead to covalent interaction. On the other hand, It has been reported repeatedly that the d-band center model can be considered as a good descriptor for the hydrogen and oxygen reactions of catalysts [43, 44]. The calculated d-band center of Co_4N and Co_3ZnN are -1.78 eV and -1.87 eV relative to the Fermi level, respectively. Therefore, the antibonding energy states are lowered and the d-band center of Co_3ZnN is more negative, far away from the Fermi level. These electronic changes might result in a weakened interaction between the material surface and hydrogen and meanwhile facilitates the desorption of hydrogen from the catalyst surface [17], which in parallel to the metal-like properties of this transition metal nitride could make the cornerstone of their excellent catalytic activity.

The possible mechanism of photocatalytic hydrogen evolution in the Eosin Y-sensitized Co_3ZnN/C nanocomposites in the TEOA aqueous solution system can be speculated like **Fig. S14**. Eosin Y (EY) is excited by the visible light and forms the singlet excited state (EY^{1*}). And then EY^{1*} changed into the triplet excited state EY^{3*} through fast intersystem crossing (ISC). In the presence of sacrificial donor TEOA, EY^{3*} is then reductively quenched to $EY^{-\cdot}$[45]. The electrons of $EY^{-\cdot}$ species are stored by the carbon black with high electronic storage capacity and then transferred to Co_3ZnN nanoparticles on the surface of carbon black, while the EY^- changing back to EY due to the loss of the electron. The electrons finally reduce H_2O to H_2 on the bimetallic active sites of Co_3ZnN nanoparticles.

3. Conclusions

In summary, an antiperovskite phase Co_3ZnN has been synthesized for efficient hydrogen evolution in the Eosin Y-sensitized system. The replacement of cobalt atom by zinc atom leads

to an improved charge transfer kinetics and catalytic properties compared with Co_4N. Carbon black support further reduces the particle size of Co_3ZnN and assists in the electron storage and adsorption capabilities. The optimal Co_3ZnN/C catalysts exhibit the H_2 evolution rate of 15.4 μmol mg^{-1} h^{-1}, which is over 6 times higher than that of monometallic Co_4N. This work is expected to provide a new guideline for optimizing transition metal nitride to realize their efficient exploitation for solar energy conversion.

4. Experimental Section

4.1 Synthesis of Co_3ZnN/C nanocomposites

Different quality $Co(NO_3)_2 \cdot 6H_2O$ and $Zn(NO_3)_2 \cdot 6H_2O$ (The molar ratio is 3:1) were dissolved in 100 mL ethanol to get the CoZn-precursor salt solution. 100 mg Carbon black were added into the CoZn-precursor salt solution and dispersed using ultrasound for 30 min. Then the liquid was dried under a constant temperature of 90 ^oC. The as-prepared precursor sample was left in a beaker and dried in a vacuum oven at 80 ^oC overnight. The dried CoZn/C precursor samples were transferred into a quartz boat after grinding and spread thinly on the boat. The samples were prepared in NH_3 flow (99.999%) of 100 sccm at 600 ^oC with a heating rate of 5 ^oC min^{-1}, and the maintained time is 1h. The black sample is the Co_3ZnN/C nanocomposites. The samples with different carbon content were prepared by controlling the mass ratio of carbon to the nitrate (Co_3ZnN/C (mass ratio 2:1), Co_3ZnN/C (mass ratio 1:1) and Co_3ZnN/C (mass ratio 1:2)). The schematic illustration is shown in Scheme S1. The reagents and the synthesis of the other contrast samples are shown in the Supplementary Information (**SI**).

4.2 Material characterization

The crystal structure for solid samples was characterized using an X-ray diffractometer (XRD, Rigaku Miniflex 600, Japan) in the 2θ range of 10-80° at a scan rate of 1° min^{-1}. Raman spectra were obtained on a confocal microprobe Raman system (Renishaw inVia Reflex). The diffuse reflectance spectra of the samples were measured in the range of 200-800 nm using a UV-vis spectrophotometer (UV-vis DRS, Hitachi U-3900, Japan) equipped with an integrating sphere attachment. Photoluminescence (PL) spectra of the different samples were investigated using a spectrophotometer (PL, Horiba Jobin Yvon Fluoromax 4C-L, France) with an excitation wavelength of 420 nm. To ensure the comparability of the PL spectra, the experimental parameters, including the excitation wavelength, slit width, and the amount of the samples, were identical. PL emission spectra of the catalysts- Eosin Y -TEOA suspensions at pH = 11 subjected to a 420 nm excitation. The concentration of Eosin Y and catalysts are 250 ppm and 0.0625 mg/mL, which are identical to the photocatalytic reaction condition. Brunauer–Emmett–Teller (BET, Micromeritics ASAP 2010, USA) surface areas were determined at 77 K. Morphologies of the samples were characterized using a field-emission scanning electron microscope (FE-SEM, Hitachi S4800, Japan). The transmission electron microscopy (TEM) and high-resolution transmission electron microscopy (HRTEM) images were obtained using a Tecnai F20 instrument. The H_2-TPD tests were carried out using a Micromeritics Autochem 2920 apparatus with a thermal conductivity detector (TCD). X-ray photoelectron spectroscopy (XPS) was performed using an AXIS Ultra DLD (Shimadzu, Japan) spectrometer with Al K α excitation (1486.6 eV).

4.3 Photoactivity testing

Photocatalytic water splitting to H_2 was carried out in a Pyrex top-irradiation reaction vessel connected to a glass closed gas circulation system. H_2 evolution analysis was performed by

dispersing 5 mg of catalyst powder and a certain quality of Eosin Y in 80 mL aqueous solution containing 8 mL TEOA (TEOA as the sacrificial electron donor). A 300 W Xe arc lamp (PLS-SXE 300, Beijing Perfect Light Co., Ltd.) was applied as the light source, and visible light irradiation was realized by using a 400 nm cutoff filter. Continuous magnetic stirring was applied at the bottom of the reactor in order to keep the photocatalyst in suspension during the whole experiments. The temperature of the reaction solution was maintained at 278 K by a flow of cooling water during the reaction. The evolved H_2 was in situ monitored periodically using an online gas chromatograph with a thermal conductivity detector (FULI GC9790II, Ar as carrier gas). The details of the recycling test are shown in **SI**.

4.4 Electrochemical measurements and computational details

The electrochemical measurements and computational details are shown in **SI**.

Acknowledgment

This work is supported by the Natural Science Foundation of China (Grant No. 21471147 and 61971405). Minghui Yang would like to thank the Ningbo 3315 program and the Opened Fund of the State Key Laboratory on Integrated Optoelectronics (No. IOSKL2017KF08) for support. Siqi Liu would like to thank for the Natural Science Foundation of Zhejiang Province (LQ19B030001).

References

[1] A. Fujishima, K. Honda, Electrochemical Photolysis of Water at a Semiconductor Electrode, Nature 238 (1972) 37-38.

[2] J. Gong, C. Li, M.R. Wasielewski, Advances in solar energy conversion, Chem. Soc. Rev. 48 (2019) 1862-1864.

[3] E. Reisner, D.J. Powell, C. Cavazza, J.C. Fontecilla-Camps, F.A. Armstrong, Visible Light-Driven H_2 Production by Hydrogenases Attached to Dye-Sensitized TiO_2 Nanoparticles, J. Am. Chem. Soc. 131 (2009) 18457-18466.

[4] C. Zhu, D. Du, A. Eychmüller, Y. Lin, Engineering Ordered and Nonordered Porous Noble Metal Nanostructures: Synthesis, Assembly, and Their Applications in Electrochemistry, Chem. Rev. 115 (2015) 8896-8943.

[5] X. Chen, S. Shen, L. Guo, S.S. Mao, Semiconductor-based Photocatalytic Hydrogen Generation, Chem. Rev. 110 (2010) 6503-6570.

[6] M.-S. Balogun, Y. Huang, W. Qiu, H. Yang, H. Ji, Y. Tong, Updates on the development of nanostructured transition metal nitrides for electrochemical energy storage and water splitting, Mater. Today 20 (2017) 425-451.

[7] L. Yu, Q. Zhu, S. Song, B. McElhenny, D. Wang, C. Wu, Z. Qin, J. Bao, Y. Yu, S. Chen, Z. Ren, Non-noble metal-nitride based electrocatalysts for high-performance alkaline seawater electrolysis, Nat. Commun. 10 (2019) 5106.

[8] A.M. Alexander, J.S. Hargreaves, Alternative catalytic materials: carbides, nitrides, phosphides and amorphous boron alloys, Chem. Soc. Rev. 39 (2010) 4388-4401.

[9] X. Lu, T. Liu, T. Zhai, G. Wang, M. Yu, S. Xie, Y. Ling, C. Liang, Y. Tong, Y. Li, Improving the Cycling Stability of Metal-Nitride Supercapacitor Electrodes with a Thin Carbon Shell, Adv. Energy Mater. 4 (2014) 1300994.

[10] S. Dong, X. Chen, X. Zhang, G. Cui, Nanostructured transition metal nitrides for energy storage and fuel cells, Coord. Chem. Rev. 257 (2013) 1946-1956.

[11] S.T. Oyama, Preparation and catalytic properties of transition metal carbides and nitrides, Catal. Today 15 (1992) 179-200.

[12] S. Gong, Z. Jiang, P. Shi, J. Fan, Q. Xu, Y. Min, Noble-metal-free heterostructure for efficient hydrogen evolution in visible region: Molybdenum nitride/ultrathin graphitic carbon nitride, Appl. Catal. B-Environ. 238 (2018) 318-327.

[13] Z. Sun, H. Chen, L. Zhang, D. Lu, P. Du, Enhanced photocatalytic H_2 production on cadmium sulfide photocatalysts using nickel nitride as a novel cocatalyst, J. Mater. Chem. A 4 (2016) 13289-13295.

[14] L. Liang, X. Li, J. Zhang, P. Ling, Y. Sun, C. Wang, Q. Zhang, Y. Pan, Q. Xu, J. Zhu, Y. Luo, Y. Xie, Efficient infrared light induced CO_2 reduction with nearly 100% CO selectivity enabled by metallic CoN porous atomic layers, Nano Energy 69 (2020) 104421.

[15] T. Varga, G. Ballai, L. Vásárhelyi, H. Haspel, Á. Kukovecz, Z. Kónya, Co4N/nitrogen-doped graphene: A non-noble metal oxygen reduction electrocatalyst for alkaline fuel cells, Appl. Catal. B-Environ. 237 (2018) 826-834.

[16] Y. Yuan, J. Wang, S. Adimi, H. Shen, T. Thomas, R. Ma, J.P. Attfield, M. Yang, Zirconium nitride catalysts surpass platinum for oxygen reduction, Nat. Mater. 19 (2020) 282-286.

[17] Z. Chen, Y. Song, J. Cai, X. Zheng, D. Han, Y. Wu, Y. Zang, S. Niu, Y. Liu, J. Zhu, X. Liu, G. Wang, Tailoring the d-Band Centers Enables Co_4N Nanosheets To Be Highly Active for Hydrogen Evolution Catalysis, Angew. Chem. Int. Ed. 57 (2018) 5076-5080.

[18] W. Qi, Y. Zhou, S. Liu, H. Liu, L.S. Hui, A. Turak, J. Wang, M. Yang, Oxidized impurity in transition metal nitride for improving the hydrogen evolution efficiency of transition metal nitride-based catalyst, Appl. Mater. Today 18 (2020) 100476.

[19] B. Cao, G.M. Veith, J.C. Neuefeind, R.R. Adzic, P.G. Khalifah, Mixed Close-Packed Cobalt Molybdenum Nitrides as Non-noble Metal Electrocatalysts for the Hydrogen Evolution Reaction, J. Am. Chem. Soc. 135 (2013) 19186-19192.

[20] K.T. Lai, I. Antonyshyn, Y. Prots, M. Valldor, Anti-Perovskite Li-Battery Cathode Materials, J. Am. Chem. Soc. 139 (2017) 9645-9649.

[21] T. He, Q. Huang, A.P. Ramirez, Y. Wang, K.A. Regan, N. Rogado, M.A. Hayward, M.K. Haas, J.S. Slusky, K. Inumara, H.W. Zandbergen, N.P. Ong, R.J. Cava, Superconductivity in the non-oxide perovskite $MgCNi_3$, Nature 411 (2001) 54-56.

[22] H. Zhang, W. Xia, H. Shen, W. Guo, Z. Liang, K. Zhang, Y. Wu, B. Zhu, R. Zou, Antiperovskite Intermetallic Nanoparticles for Enhanced Oxygen Reduction, Angew. Chem. Int. Ed. 59 (2020) 1871-1877.

[23] J. Sheng, L. Wang, L. Deng, M. Zhang, H. He, K. Zeng, F. Tang, Y.N. Liu, MOF-Templated Fabrication of Hollow Co_4N@N-Doped Carbon Porous Nanocages with Superior Catalytic Activity, ACS Appl. Mater. Interfaces 10 (2018) 7191-7200.

[24] Y. Yang, R. Zeng, Y. Xiong, F.J. DiSalvo, H.D. Abruna, Cobalt-Based Nitride-Core Oxide-Shell Oxygen Reduction Electrocatalysts, J. Am. Chem. Soc. 141 (2019) 19241-19245.

[25] R.-Q. Li, P. Hu, M. Miao, Y. Li, X.-F. Jiang, Q. Wu, Z. Meng, Z. Hu, Y. Bando, X.-B. Wang, CoO-modified Co_4N as a heterostructured electrocatalyst for highly efficient overall water splitting in neutral media, J. Mater. Chem. A 6 (2018) 24767-24772.

[26] Z. Li, Y. Cui, Z. Wu, C. Milligan, L. Zhou, G. Mitchell, B. Xu, E. Shi, J.T. Miller, F.H. Ribeiro, Y. Wu, Reactive metal-support interactions at moderate temperature in two-dimensional niobium-carbide-supported platinum catalysts, Nat. Catal. 1 (2018) 349-355.

[27] M. Roca-Ayats, G. García, J.L. Galante, M.A. Peña, M.V. Martínez-Huerta, TiC, TiCN, and TiN Supported Pt Electrocatalysts for CO and Methanol Oxidation in Acidic and Alkaline Media, J. Phys. Chem. C 117 (2013) 20769-20777.

[28] I.-C. Kang, Q. Zhang, S. Yin, T. Sato, F. Saito, Improvement in Photocatalytic Activity of TiO2 under Visible Irradiation through Addition of N-TiO_2, Environ. Sci. Technol. 42 (2008) 3622-3626.

[29] Y. Yuan, L. Yang, B. He, E. Pervaiz, Z. Shao, M. Yang, Cobalt-zinc nitride on nitrogen doped carbon black nanohybrids as a non-noble metal electrocatalyst for oxygen reduction reaction, Nanoscale 9 (2017) 6259-6263.

[30] J. Swaminathan, A.B. Puthirath, M.R. Sahoo, S.K. Nayak, G. Costin, R. Vajtai, T. Sharifi, P.M. Ajayan, Tuning the Electrocatalytic Activity of Co_3O_4 through Discrete Elemental Doping, ACS Appl. Mater. Interfaces 11 (2019) 39706-39714.

[31] I.K. Moon, S. Yoon, B. Ki, K. Choi, J. Oh, Remarkable Enhancement of Electrochemical Performance by the Oxygen Vacancy and Nitrogen Doping in $ZnCo_2O_4$ Nanowire Arrays, ACS Appl. Energy Mater. 1 (2018) 4804-4813.

[32] S.H. Li, N. Zhang, X. Xie, R. Luque, Y.J. Xu, Stress-Transfer-Induced In Situ Formation of Ultrathin Nickel Phosphide Nanosheets for Efficient Hydrogen Evolution, Angew. Chem. Int. Ed. 57 (2018) 13082-13085.

[33] B. Pan, Y. Wu, J. Qin, C. Wang, Ultrathin $Co_{0.85}Se$ nanosheet cocatalyst for visible-light CO_2 photoreduction, Catal. Today 335 (2019) 208-213.

[34] F. Meng, J. Li, S.K. Cushing, M. Zhi, N. Wu, Solar hydrogen generation by nanoscale p-n junction of p-type molybdenum disulfide/n-type nitrogen-doped reduced graphene oxide, J. Am. Chem. Soc. 135 (2013) 10286-10289.

[35] N. Zhang, M.-Y. Qi, L. Yuan, X. Fu, Z.-R. Tang, J. Gong, Y.-J. Xu, Broadband Light Harvesting and Unidirectional Electron Flow for Efficient Electron Accumulation for Hydrogen Generation, Angew. Chem. Int. Ed. 58 (2019) 10003-10007.

[36] S. Wang, B.Y. Guan, L. Yu, X.W.D. Lou, Rational Design of Three-Layered TiO_2 @Carbon@MoS_2 Hierarchical Nanotubes for Enhanced Lithium Storage, Adv. Mater. 29 (2017) 1702724.

[37] B. Ma, X. Li, D. Li, K. Lin, A difunctional photocatalytic H_2 evolution composite co-catalyst tailored by integration with earth-abundant material and ultralow amount of noble metal, Appl. Catal. B-Environ. 256 (2019) 117865.

[38] Z. Liu, H. Tan, J. Xin, J. Duan, X. Su, P. Hao, J. Xie, J. Zhan, J. Zhang, J.J. Wang, H. Liu, Metallic Intermediate Phase Inducing Morphological Transformation in Thermal Nitridation: Ni_3FeN-Based Three-Dimensional Hierarchical Electrocatalyst for Water Splitting, ACS Appl. Mater. Interfaces 10 (2018) 3699-3706.

[39] C.H. Hao, X.N. Guo, M. Sankar, H. Yang, B. Ma, Y.F. Zhang, X.L. Tong, G.Q. Jin, X.Y. Guo, Synergistic Effect of Segregated Pd and Au Nanoparticles on Semiconducting SiC for Efficient Photocatalytic Hydrogenation of Nitroarenes, ACS Appl. Mater. Interfaces 10 (2018) 23029-23036.

[40] L. Zhou, Z. Zhuo, L. Kou, A. Du, S. Tretiak, Computational Dissection of Two-Dimensional Rectangular Titanium Mononitride TiN: Auxetics and Promises for Photocatalysis, Nano Lett. 17 (2017) 4466-4472.

[41] Y. Gu, S. Chen, J. Ren, Y.A. Jia, C. Chen, S. Komarneni, D. Yang, X. Yao, Electronic Structure Tuning in Ni_3FeN/r-GO Aerogel toward Bifunctional Electrocatalyst for Overall Water Splitting, ACS Nano 12 (2018) 245-253.

[42] X. Zhang, Y. Zhao, X. Jia, Y. Zhao, L. Shang, Q. Wang, G.I.N. Waterhouse, L.-Z. Wu, C.-H. Tung, T. Zhang, Silica-Protected Ultrathin Ni_3FeN Nanocatalyst for the Efficient Hydrolytic Dehydrogenation of NH_3BH_3, Adv. Energy Mater. 8 (2018) 1702780.

[43] H. Xin, A. Vojvodic, J. Voss, J.K. Nørskov, F. Abild-Pedersen, Effects ofd-band shape on the surface reactivity of transition-metal alloys, Phys. Rev. B 89 (2014).

[44] B. Hammer, J.K. Norskov, Electronic factors determining the reactivity of metal surfaces, Surf. Sci. 343 (1995) 211-220.

[45] L. Yang, J. Huang, L. Shi, L. Cao, W. Zhou, K. Chang, X. Meng, G. Liu, Y. Jie, J. Ye, Efficient hydrogen evolution over Sb doped SnO_2 photocatalyst sensitized by Eosin Y under visible light irradiation, Nano Energy 36 (2017) 331-340.

Captions of Figures

Fig. 1 The Rietveld-fitted X-ray powder diffraction pattern of (a) Co_3ZnN and (b) Co_4N in ammonia at 600 ^oC. Charge density distribution of (200) surface in (c) Co_3ZnN and (d) Co_4N, respectively. More negative charge can be observed at N-Co-N network in Co_3ZnN than that in Co_4N.

Fig. 2 TEM images and HRTEM images of (a,b) bulk Co_3ZnN and (c,d) Co_3ZnN/C(1:1) nanocomposites.

Fig. 3 The XPS spectra of Co_4N, Co_3ZnN and Co_3ZnN/C(1:1) in the (a) Co 2p, (b) Zn 2p and (c) N1s regions. (d) The Raman spectrum of as-prepared catalysts.

Fig. 4 (a) The average rates of H_2 evolution under visible-light ($\lambda > 400$ nm) over as-prepared Co_4N, Co_3ZnN and Co_3ZnN/C (1:1) samples in Eosin Y-TEOA system. (b) LSV curves of the as-prepared samples, the blank GCDE (electrode rotating speed, 1600 r.p.m.; scan rate, 100 mV s^{-1}). (c) Electrochemical impedance spectra of Co_4N, Co_3ZnN and Co_3ZnN/C(1:1) (AC voltage, -1.5 V; frequency range, from 10000 Hz to 0.1 Hz). (d) H_2-TPD profiles of Co_4N and Co_3ZnN/C(1:1) samples.

Fig. 5 The atomic structure model of (a) Co_4N and (b) Co_3ZnN. The large pink and large gray balls show Co and Zn atoms respectively, and the O atom is shown by a small turquoise ball. The electronic structure of (c) Co_4N and (d) Co_3ZnN. Calculated electronic densities of states of (e) Co_4N and (f) Co_3ZnN. The Fermi level is set to zero.

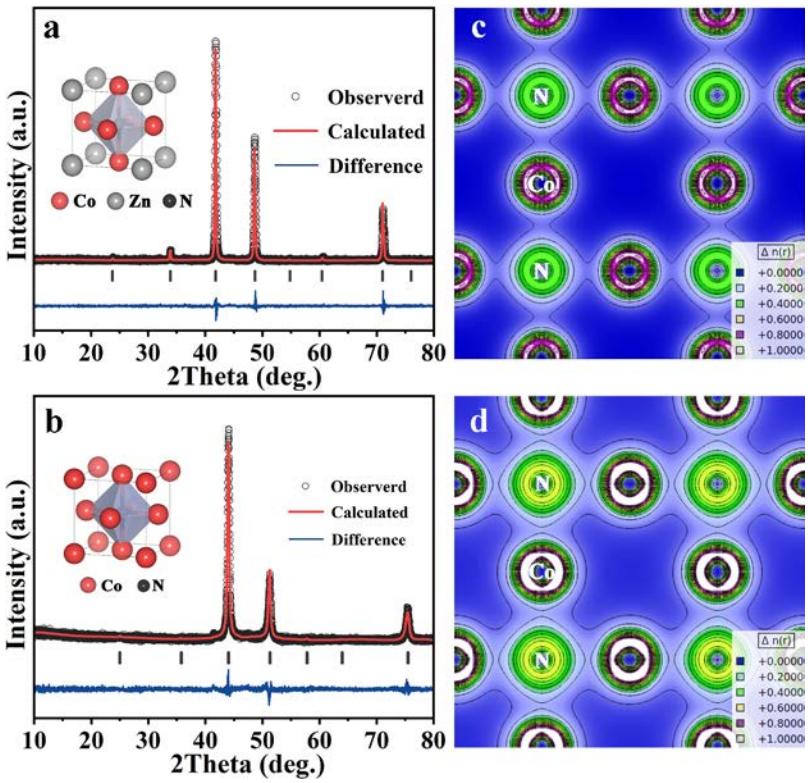

Fig. 1 The Rietveld-fitted X-ray powder diffraction pattern of (a) Co_3ZnN and (b) Co_4N in ammonia at 600 ^oC. Charge density distribution of (200) surface in (c) Co_3ZnN and (d) Co_4N, respectively. More negative charge can be observed at N-Co-N network in Co_3ZnN than that in Co_4N.

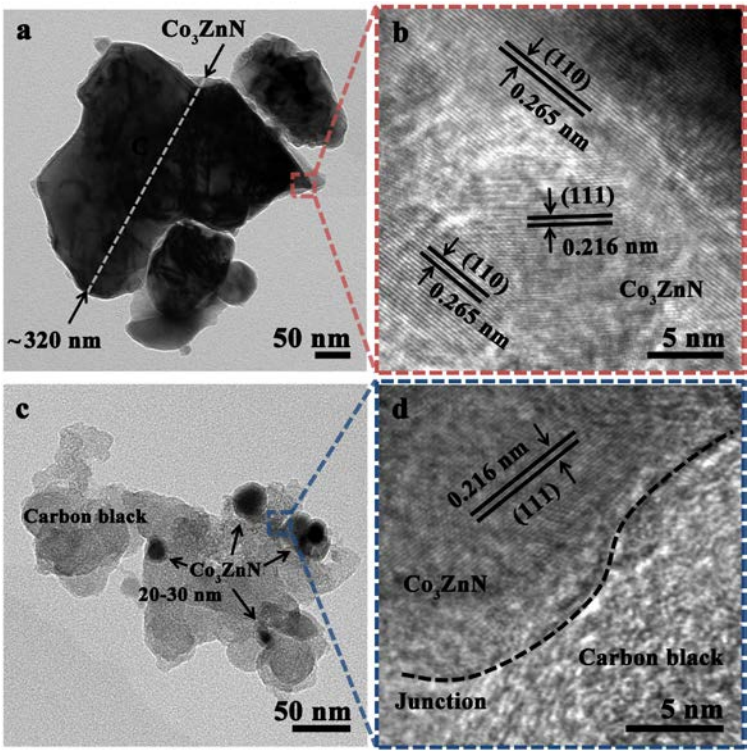

Fig. 2 TEM images and HRTEM images of (a,b) bulk Co_3ZnN and (c,d) Co_3ZnN/C(1:1) nanocomposites.

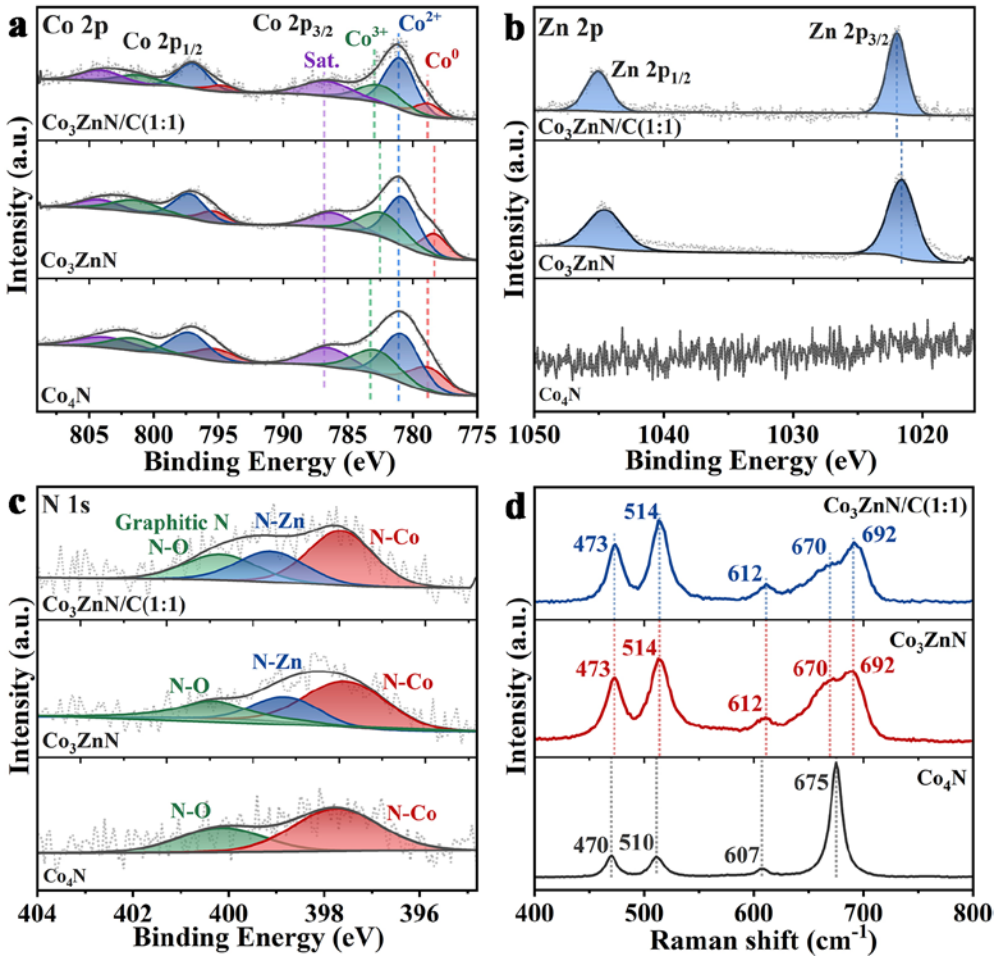

Fig. 3 The XPS spectra of Co_4N, Co_3ZnN and $Co_3ZnN/C(1:1)$ in the (a) Co 2p, (b) Zn 2p and (c) N1s regions. (d) The Raman spectrum of as-prepared catalysts.

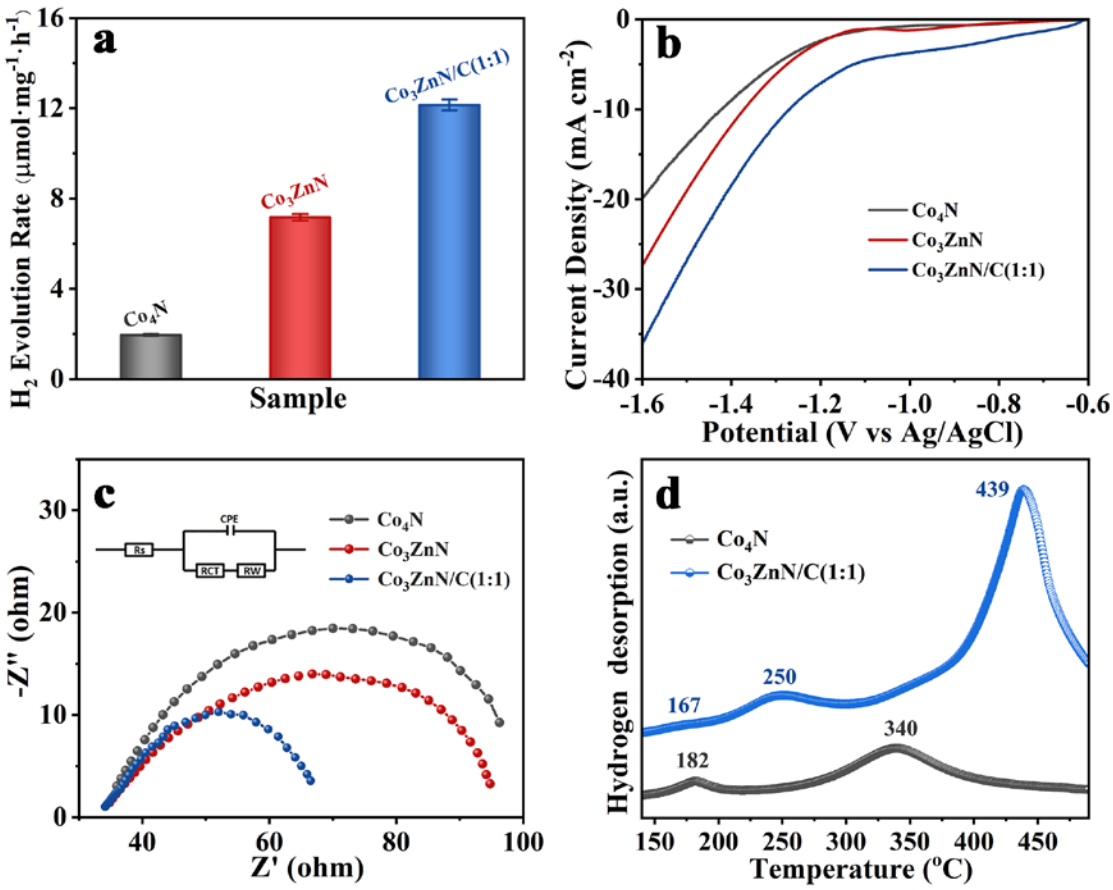

Fig. 4 (a) The average rates of H_2 evolution under visible-light ($\lambda > 400$ nm) over as-prepared Co_4N, Co_3ZnN and Co_3ZnN/C (1:1) samples in Eosin Y-TEOA system. (b) LSV curves of the as-prepared samples, the blank GCDE (electrode rotating speed, 1600 r.p.m.; scan rate, 100 mV s^{-1}). (c) Electrochemical impedance spectra of Co_4N, Co_3ZnN and $Co_3ZnN/C(1:1)$ (AC voltage, -1.5 V; frequency range, from 10000 Hz to 0.1 Hz). (d) H_2-TPD profiles of Co_4N and $Co_3ZnN/C(1:1)$ samples.

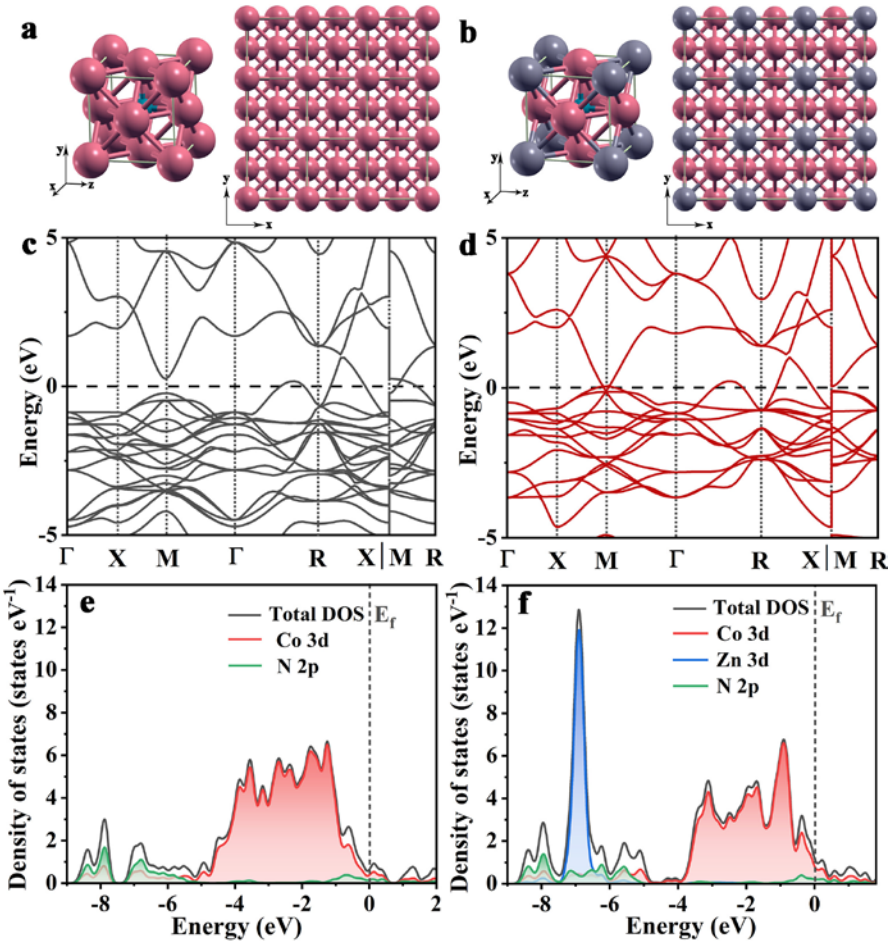

Fig. 5 The atomic structure model of (a) Co_4N and (b) Co_3ZnN. The large pink and large gray balls show Co and Zn atoms respectively, and the O atom is shown by a small turquoise ball. The electronic structure of (c) Co_4N and (d) Co_3ZnN. Calculated electronic densities of states of (e) Co_4N and (f) Co_3ZnN. The Fermi level is set to zero.